

# Elevated foehn exacerbates surface ozone pollution in summer Beijing

Zhiheng Liao<sup>1</sup>, Jing Xu<sup>1</sup>, Ju Li<sup>1</sup>, Liyan Zhou<sup>1</sup>, Chao Liu<sup>1</sup>, Lin Wu<sup>2</sup>, Zhiqiang Ma<sup>1</sup>

<sup>1</sup>Institute of Urban Meteorology, China Meteorological Administration, Beijing, China;

<sup>2</sup>Huairou Meteorological Office of Beijing, Beijing, China.

Correspondence: Z. Liao (zhliao@ium.cn) and Z. Ma (zqma@ium.cn)

**Abstract:** While several studies have evaluated the impact of shallow foehn on air pollution, the effects of elevated foehn on O<sub>3</sub> pollution remain poorly understood. Here, we investigate the role of elevated foehn in summer O<sub>3</sub> pollution in Beijing through detailed case analysis and a long-term climatological evaluation. The case study reveals that elevated foehn exacerbates next-day O<sub>3</sub> pollution through three primary mechanisms: first, by increasing boundary layer temperature, thereby enhancing photochemical O<sub>3</sub> formation; second, by reducing the residual/boundary layer height, thereby inhibiting vertical diffusion of pollutants; and third, by slowing boundary layer winds, thereby suppressing horizontal dispersion. A ten-year climatological evaluation of 54 identified elevated foehn events strongly supports these mechanisms. On average, these events led to a post-foehn afternoon boundary layer temperature increase exceeding 3°C, an afternoon boundary layer height reduction of more than 100 m, and a decrease in afternoon boundary layer wind speed of more than 1.0 m s<sup>-1</sup> compared to the pre-foehn days. Consequently, 87% of elevated foehn events were associated with a worsening of O<sub>3</sub> pollution. Post-foehn daily maximum 8-hour average O<sub>3</sub> concentrations frequently surpassed the national pollution threshold (160 µg m<sup>-3</sup>), with an average increase of 20%–60% (varying by site and higher in urban areas) compared to preceding days. These results demonstrate a robust and deterministic exacerbating effect of elevated foehn on surface O<sub>3</sub> pollution, suggesting that elevated foehn can serve as a reliable meteorological precursor for O<sub>3</sub> pollution warnings in summer Beijing.

**Keywords:** elevated foehn, atmospheric boundary layer, residual layer warming, ozone pollution, Beijing

## 1. Introduction

Foehn is a phenomenon of downslope winds with significant warming on the mountain leeward side (Elvidge and Renfrew, 2016). It has been observed among many large mountains in the world, including the Alpine Mountains (Miltenberger et al., 2016; Seibert et al., 2000), Rocky Mountains (Kerr, 1986), Appalachian Mountains (Gaffin, 2002, 2009), Taihang Mountains (Li et al., 2020a; Li et al., 2025), and Tianshan Mountains (Li et al., 2015; Li et al., 2020b). The societal and economic impacts of foehn winds are wide-ranging and well-documented, encompassing enhanced fire risks, extreme heat exposure, impacts on air quality, beneficial impacts on agriculture, and direct wind-driven damage to infrastructure. Given these multifaceted impacts, foehn has long been a subject of sustained scholarly interest across diverse disciplines.

Scientific research into the effect of foehn on air pollution began in Europe in the late nineteenth century, primarily to explain elevated ozone (O<sub>3</sub>) levels in the Alpine regions during foehn events (Baumann et al., 2001; Campana et al., 2005; Seibert et al., 2000). Early European studies identified that the initial rise in O<sub>3</sub> concentration was caused by the advection of residual-layer air masses from source regions such as the Po Basin. Later on, O<sub>3</sub> levels in the foehn-affected area were found to be influenced by regional-scale advection from the lower free troposphere or even the stratosphere. Collectively, these studies emphasized the transport role of foehn in influencing O<sub>3</sub> air quality in the relatively clean valleys of Alps. In contrast, research in China has commonly demonstrated a “clearance effect”

45 of foehn on air pollution in highly-polluted cities (Li et al., 2020a; Li et al., 2025; Yang et al., 2018). For example,  
46 Yang et al. (2018) reported a case in Shijiazhuang where foehn led to rapidly improved horizontal visibility, decreased  
47 aerosol concentration, and weakened haze intensity. Similarly, a six-year statistical study by Li et al. (2025) found  
48 that 60.4 % of foehn events were associated with a subsequent decrease in fine particulate matter (PM<sub>2.5</sub>)  
49 concentrations in Beijing. This clearance effect is attributed to the origin of the foehn winds, which typically transport  
50 cleaner air from the less polluted western, northwestern and northern mountain areas of the Hebei–Beijing region  
51 into more polluted plains.

52

53 These abovementioned studies, conducted in both Europe and China, primarily examine the foehn effect on air  
54 pollution mainly from a dynamical (transport) perspective. Furthermore, the foehn cases selected in these studies are  
55 generally confined to shallow foehns, identifying using near-surface meteorological observations. Crucially, however,  
56 the defining feature of foehn is the associated warming (Elvidge and Renfrew, 2016). This warming inevitably alters  
57 the vertical thermal structure—and thus the atmospheric stability—which directly governs the capacity for vertical  
58 diffusion of air pollutants (Liao et al., 2018; Stull, 1988). Therefore, the vertical extent of the foehn (shallow or  
59 elevated) critically determines its impact on atmospheric stability: shallow foehn tends to enhance near-surface  
60 instability, while elevated foehn can strengthen stability within or above the boundary layer. From this  
61 thermodynamic perspective, elevated foehn likely possesses a greater pollution potential than its shallow counterpart.  
62 Despite this reasoning, to the best of our knowledge, only one study—Li et al. (2015) in Urumqi, a city adjacent to  
63 Tianshan Mountains—has explicitly investigated the impact of an elevated foehn on air pollution from a  
64 thermodynamic viewpoint. That study revealed that an elevated southeasterly foehn layer between 480 and 2100 m  
65 created a very stable boundary layer structure, which suppressed vertical mixing and led to severe haze pollution  
66 episodes. Recent studies on PM<sub>2.5</sub> pollution in Beijing (Li et al., 2020a; Li et al., 2025) have speculated that post-  
67 foehn pollution exacerbation might be driven by a mechanism similar to the elevated foehn process observed in  
68 Urumqi (Li et al., 2015). However, the existence and role of such an elevated foehn mechanism have not yet been  
69 observationally confirmed for Beijing.

70

71 Beijing, the capital of China, faces significant challenges in terms of air pollution. Particularly in recent summers,  
72 O<sub>3</sub> has surpassed PM<sub>2.5</sub> as the most important air pollutant, arousing widespread attention (Liao et al., 2023; Zong et  
73 al., 2023). The city's location on the plains adjacent to the Taihang Mountains to the west and the Yan Mountains to  
74 the north makes it particularly susceptible to foehn winds (Xu et al., 2026). Luo et al. (2020) documented an intensive  
75 foehn warming event in Beijing where nocturnal air temperatures increased by over 10°C per hour. Utilizing data  
76 from a density automatic weather station network, Li et al. (2025) developed a foehn identification method and  
77 reported an annual average of 56.5 foehn days in Beijing. As noted earlier, their statistical analysis suggests a higher  
78 probability of PM<sub>2.5</sub> pollution alleviation (60.4 %) rather than pollution exacerbation (39.6 %) following foehn events  
79 in Beijing. Importantly, because their identification method only relies on near-surface observations, the detected  
80 events are predominantly shallow foehns. This methodological focus may obscure the distinct air pollution effects  
81 potentially caused by elevated foehns. Therefore, determining whether elevated foehn induces a more deterministic—  
82 and likely adverse—pollution effects is a critical unanswered question. The answer has practical importance, as it  
83 would inform whether elevated foehn can serve as a reliable precursor indicator for air pollution warnings, thereby  
84 improving mitigation efforts in Beijing and other leaside cities.

85

86 To address this knowledge gap, our team deployed two O<sub>3</sub> lidars at an urban (Guanxiangtai, GXT) and a rural  
87 (Shangdianzi, SDZ) station in Beijing in late July 2024. This coordinated dual-station lidar setup is particularly suited  
88 to capturing the three-dimensional characteristics and mechanisms of boundary layer O<sub>3</sub> evolution under the influence

89 of elevated foehn. One month after deployment (27–31 August), we observed an O<sub>3</sub> pollution episode associated with  
90 an elevated foehn. In this study, we conducted a detailed analysis of this event by integrating data from the new lidar  
91 system with co-located remote sensing meteorological observations. We supplement this case study with a  
92 climatological evaluation using a decade (2015–2024) of routine observations. Our overarching aim is to elucidate  
93 the specific role of elevated foehn in driving summer O<sub>3</sub> pollution in Beijing.

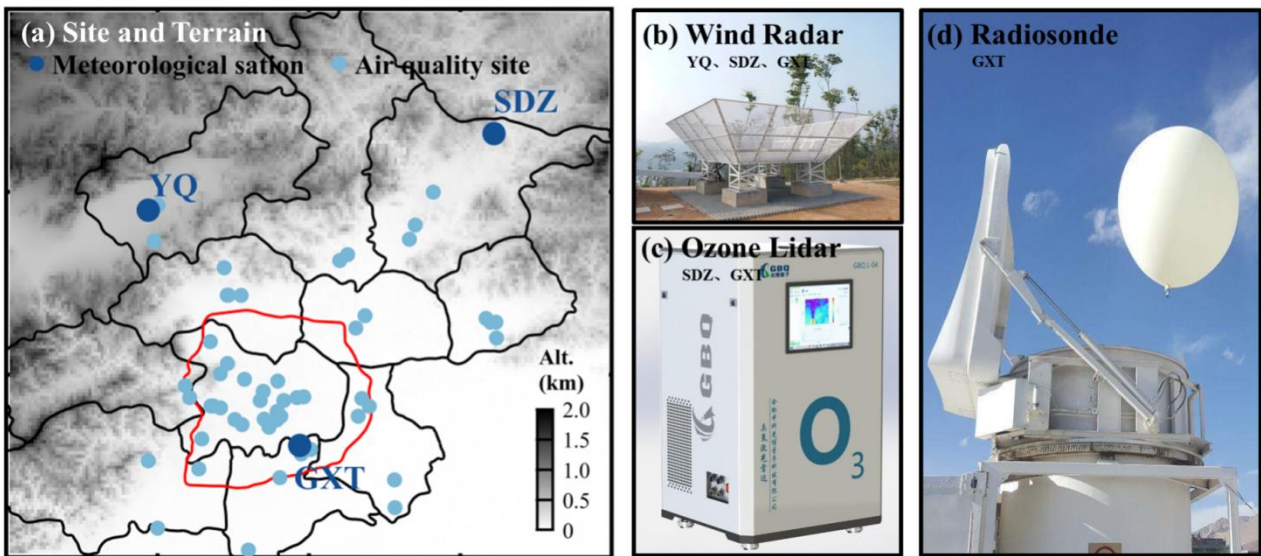
94

## 95 2. Data and method

### 96 2.1. Observational data

97 Figure 1 shows the observation network and instruments. The network comprises 3 meteorological stations and 46  
98 surface O<sub>3</sub> monitoring sites. Among the O<sub>3</sub> sites, 45 are air quality stations operated by the Beijing Municipal  
99 Ecological and Environmental Monitoring Center, and one is the Shangdianzi (SDZ) atmospheric background station  
100 managed by the Beijing Meteorological Bureau. Two differential absorption O<sub>3</sub> lidars (Hefei GBQ Technology  
101 Company) were deployed at the GXT (urban) and SDZ (rural) stations, respectively. These lidars measured O<sub>3</sub>  
102 profiles with a 5-minute resolution up to an altitude of 3.0 km. In addition, radar wind profilers at GXT, SDZ, as well  
103 as Yanqing (YQ) provided continuous wind profiles at 6-minute resolution. Routine meteorological radiosondes  
104 launched from the GXT station provided high-vertical-resolution (~10 m) profiles of temperature, relative humidity,  
105 wind speed, and wind direction three times daily (08:00, 14:00, and 20:00 BJT) in summer.

106



111

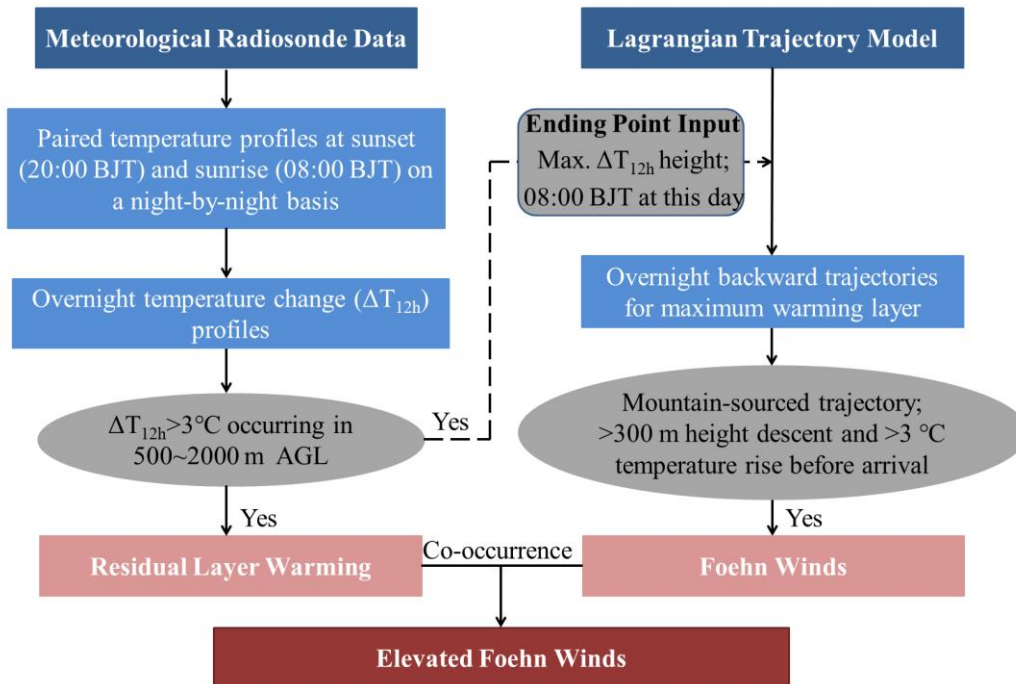
112 To validate the lidar O<sub>3</sub> observations, we compared the lidar-derived O<sub>3</sub> concentration at 300 m height (the lowest  
113 reliable altitude above the instrument's blind zone) with surface measurements. As no surface O<sub>3</sub> data were available  
114 at the GXT site, we used measurements from the nearest air quality monitoring station (~2 km away). The validation  
115 results demonstrated a strong correlation between the lidar-based and surface-based O<sub>3</sub> concentrations ( $R^2 = 0.69$  at  
116 GXT and  $R^2 = 0.56$  at SDZ), confirming the reliability of the O<sub>3</sub> lidar data (Fig. S1). To construct complete vertical  
117 profiles for calculating O<sub>3</sub> transport flux, we used linear interpolation between the surface O<sub>3</sub> measurement and the  
118 validated lidar observation at 300 m to fill the blind zone. A similar procedure was applied to patch the blind zone

119 (below 150 m) of the radar wind profiler data, where winds were interpolated between the surface wind observation  
 120 and the lowest valid radar measurement at 150 m.

121

122 **2.2. Identification of elevated foehn**

123 To date, no established method exists for identifying elevated foehn. For the purpose of climatological evaluation,  
 124 we develop a framework (Fig. 2) to identify elevated foehn events based on the combination of meteorological  
 125 radiosonde data and a Lagrangian trajectory model. First, we calculated overnight temperature change ( $\Delta T_{12h}$ ) profiles  
 126 by subtracting the radiosonde temperature profiles at 20:00 BJT (sunset) from the profiles at 08:00 BJT the following  
 127 day (sunrise) on a night-by-night basis (i.e.,  $\Delta T_{12h}=T_{08}-T_{20}$ ). A residual layer warming event was identified when  
 128  $\Delta T_{12h}>3^{\circ}\text{C}$  occurred within 500–2000 m AGL layer. This threshold is also commonly used to identify ground-based  
 129 foehn elsewhere (Kirchgaessner et al., 2021; Steinhoff et al., 2014). Finally, we examined the backward trajectory  
 130 properties (including geographic origin, height change, and temperature change) of the air mass at the identified  
 131 maximum warming height (i.e., the height of maximum  $\Delta T_{12h}$ ) using a Lagrangian trajectory model (Miltenberger et  
 132 al., 2016). If the 12-h backward trajectory originated from the mountains (azimuth of  $250\text{--}360^{\circ}$  or  $0\text{--}45^{\circ}$ , following  
 133 Li et al. (2025)), and if the trajectory descended more than 300 m accompanied by a temperature increase exceeding  
 134  $3^{\circ}\text{C}$  before arriving in Beijing, we attribute the identified warming case to an elevated foehn event.



135

136 **Figure 2.** Flowchart for identifying elevated foehn based on the combination of meteorological radiosonde data and  
 137 a Lagrangian trajectory model.

138

139 **2.3. Supporting calculations and model simulations**

140 The boundary layer structure during a diurnal cycle can be classified into three regimes: convective boundary layer  
 141 (CBL), stable boundary layer (SBL), and residual layer (RL) (Stull, 1988). We determined the boundary layer height  
 142 based on high-resolution radiosonde profiles from the GXT station. Following Liu and Liang (2010), the height of  
 143 the CBL (CBLH, at 14:00 BJT) was determined at the base of the overlying temperature inversion capping the  
 144 convective thermals. The height of the SBL (SBLH, at 20:00 and 08:00 BJT) was determined at the top of the  
 145 underlying temperature inversion, where turbulence nearly ceases. At the morning transition (08:00 BJT), emerging  
 146 solar radiation gradually erodes the near-surface part of the SBL; thus, the SBLH at this time was determined at the

147 top of the residual underlying temperature inversion. The RL is disconnected from the ground by the underlying SBL  
148 but retains the atmospheric state of the former CBL. Its height (RLH) was therefore determined at the base of the  
149 overlying temperature inversion at the evening or morning transition (20:00 and 08:00 BJT). For temperature profiles  
150 showing no significant overlying inversion, the CHLH and RLH were determined using a multi-variable integrated  
151 method proposed by Wang and Wang (2014).

152

153 To analyze O<sub>3</sub> transport in Beijing, we calculated the O<sub>3</sub> transport flux (TF) using collocated wind and O<sub>3</sub> profiles  
154 from the GXT and SDZ sites. The transport flux (TF, mg m<sup>-2</sup> s<sup>-1</sup>), representing the mass flow per unit cross-sectional  
155 area per unit time, is determined by the wind speed and the O<sub>3</sub> concentration. The TF at a certain height and direction  
156 is calculated as follow:

157 
$$TF = C \times WS \times \cos \left[ (WD - B) \times \frac{\pi}{180} \right]$$

158 where  $C$  represents the O<sub>3</sub> concentration (unit: μg m<sup>-3</sup>),  $WS$  denotes the horizontal wind speed (unit: m s<sup>-1</sup>),  $WD$   
159 denotes the horizontal wind direction and  $B$  is the azimuth from the start station to the end station. In this study, we  
160 calculated O<sub>3</sub> transport flux in the direction from GXT to SDZ. Therefore, positive TF indicates northeastward  
161 transport, and negative TF indicates southwestward transport.

162

163 We used the Hybrid Single-Particle Lagrangian Integrated Trajectory (HYSPLIT) model (Stein et al., 2015) to  
164 trace the origin and history of the air masses associated with the maximum residual layer warming in Beijing. In  
165 addition to HYSPLIT, we employed the Weather Research and Forecasting model with Chemistry (WRF-Chem,  
166 version 4.2.1) to simulate O<sub>3</sub> concentrations and meteorological fields. The WRF-Chem model accounts for key  
167 atmospheric processes, including emissions, deposition, advection, diffusion, gas-phase chemistry, and aerosol  
168 chemistry (Grell et al., 2005). Our simulation domain encompassed most of China, centered at (105.5°E, 37.5°N),  
169 with a horizontal grid spacing of 9 km. The meteorological initial and boundary conditions were derived from the  
170 National Centers for Environmental Prediction (NCEP) Final Operational Global Analysis data. For emissions, we  
171 utilized the Model of Emissions of Gases and Aerosols from Nature (MEGAN) (Guenther et al., 2006) and the Multi-  
172 resolution Emission Inventory for China (MEIC) (Zhang et al., 2009), with the latter updated to a 0.1° × 0.1°  
173 resolution for 2019 (MEIC-2019; <http://www.meicmodel.org>). The detailed model configuration follows Xu et al.  
174 (2024). The WRF-Chem simulation demonstrated a reasonable agreement with observed surface O<sub>3</sub> concentrations  
175 during the studied pollution episode ( $R^2 = 0.51$  at GXT and  $R^2 = 0.44$  at SDZ; Fig. S2).

176

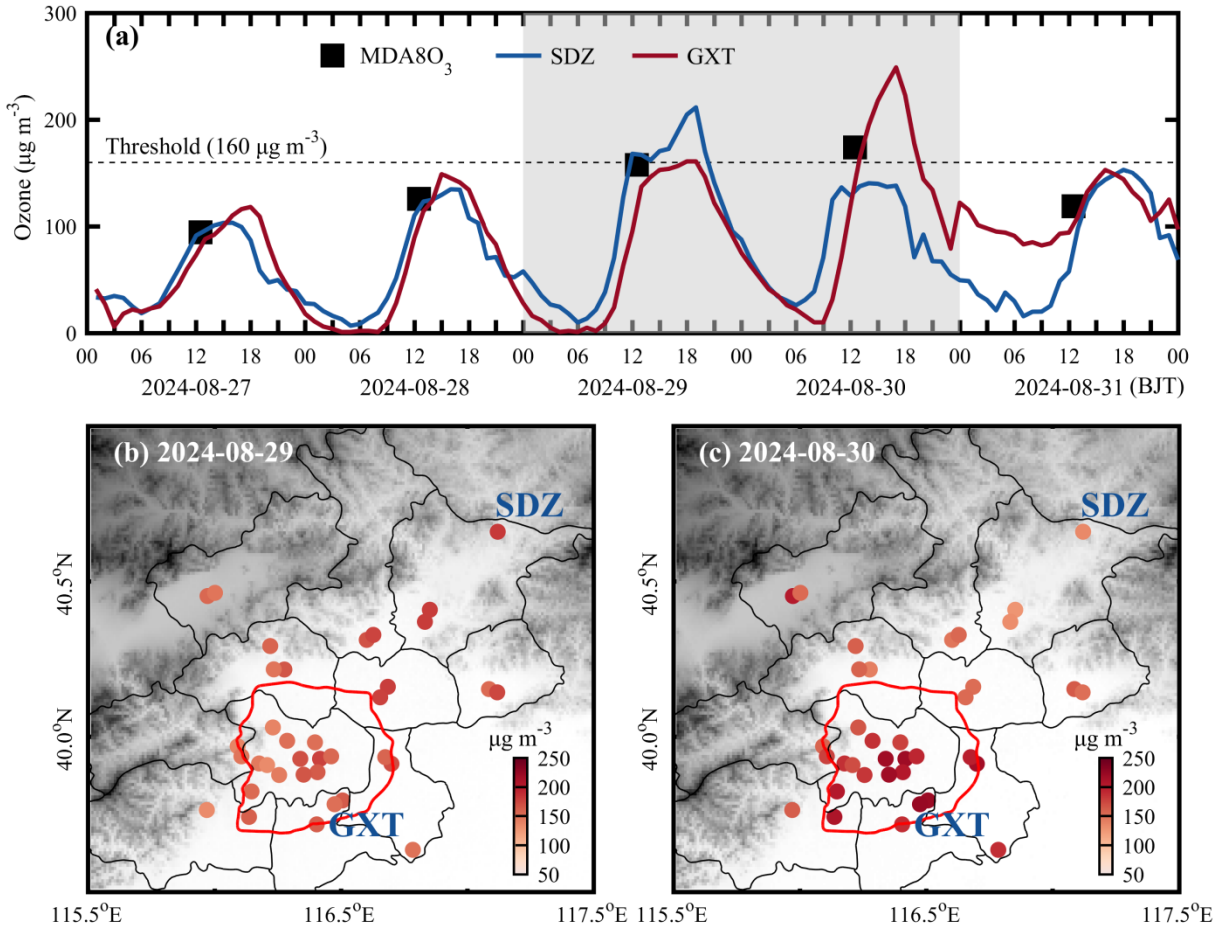
## 177 **3. Results**

### 178 **3.1. Case study**

#### 179 **3.1.1. Overview of the O<sub>3</sub> pollution episode**

180 Following heavy rainfall on 26 August 2024, Beijing experienced consecutive sunny days until light rain resumed  
181 on 31 August. The persistent sunny weather established favorable meteorological background for photochemical O<sub>3</sub>  
182 production. Consequently, surface O<sub>3</sub> concentrations in Beijing exhibited a daily increasing trend from 27 to 30  
183 August. On the final two days (29 and 30 August), the city-averaged daily maximum 8-hour average O<sub>3</sub> (MDA8O<sub>3</sub>)  
184 concentrations approached or exceeded China's ambient air quality standard threshold of 160 μg m<sup>-3</sup>, peaking at 174  
185 μg m<sup>-3</sup> on 30 August (Fig. 3a). A notable feature of these two polluted days was the stark contrast in the spatial  
186 distribution of O<sub>3</sub> concentrations. On 29 August, the spatial pattern showed a positive O<sub>3</sub> gradient extending  
187 northeastward, which was reversed on 30 August (Fig. 3b, c). This contrast was exemplified by the station  
188 observations: SDZ recorded its peak O<sub>3</sub> concentration (212 μg m<sup>-3</sup> at 18:00 BJT) on 29 August, significantly higher  
189 than the concurrent value at GXT (161 μg m<sup>-3</sup>). Conversely, GXT observed its maximum O<sub>3</sub> level (249 μg m<sup>-3</sup> at

190 16:00 BJT) on 30 August, far exceeding the measurement at SDZ ( $138 \mu\text{g m}^{-3}$ ; Fig. 3a). These contrasting spatial  
 191 patterns seem to represent two typical  $\text{O}_3$  pollution scenarios in Beijing: an urban plume transport pattern and an  
 192 urban pollution accumulation pattern, as previously reported by Zong et al. (2023). The key question is what  
 193 mechanism drove the rapid intensification of  $\text{O}_3$  pollution and the reversal of its spatial pattern over the two  
 194 consecutive days.

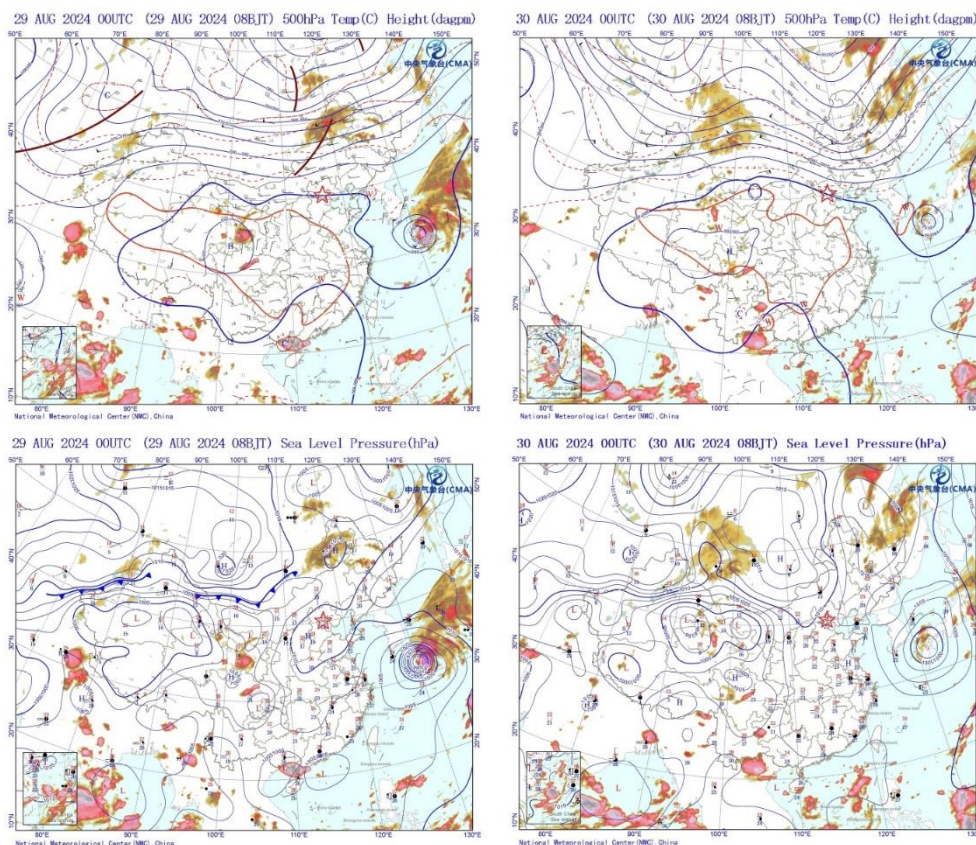


195  
 196 **Figure 3.** (a) Time series of surface ozone concentrations at the GXT and SDZ stations from 27 to 31 August 2024;  
 197 Spatial distribution of maximum 8-h  $\text{O}_3$  concentrations over Beijing on (b) 29 and (c) 30 August. In (a), black squares  
 198 represent the city-averaged  $\text{MDA8O}_3$  concentrations; gray shading denotes the two polluted days (29 and 30 August  
 199 2024).

200  
 201 **3.1.2. Meteorological attribution to elevated foehn**

202 The weather charts at 08:00 BJT on 29 and 30 August are presented in Fig. 4. A subtropical high prevailed in the  
 203 upper atmosphere over the central and eastern China, while a typhoon was active over the western Pacific Ocean  
 204 south of Japan. The coexistence of these two synoptic systems induced widespread clear skies over the eastern China,  
 205 a condition highly conducive to photochemical  $\text{O}_3$  production (Ouyang et al., 2022; Shu et al., 2016). In the lower  
 206 atmosphere, the synoptic patterns differed between the two days. On 29 August, the North China Plain (NCP) was  
 207 under the influence of a weak high-pressure system. By 30 August, another high-pressure system (a cold front) had  
 208 intruded into the northwestern NCP from the Mongolian Plateau, creating a strong pressure gradient perpendicular to  
 209 the Taihang Mountains. Traditionally, cold fronts are known to have a significant clearance effect on air pollutants  
 210 (Zhang et al., 2021). However, in this case, the cold front led to an unexpected  $\text{O}_3$  increase in Beijing on 30 August.

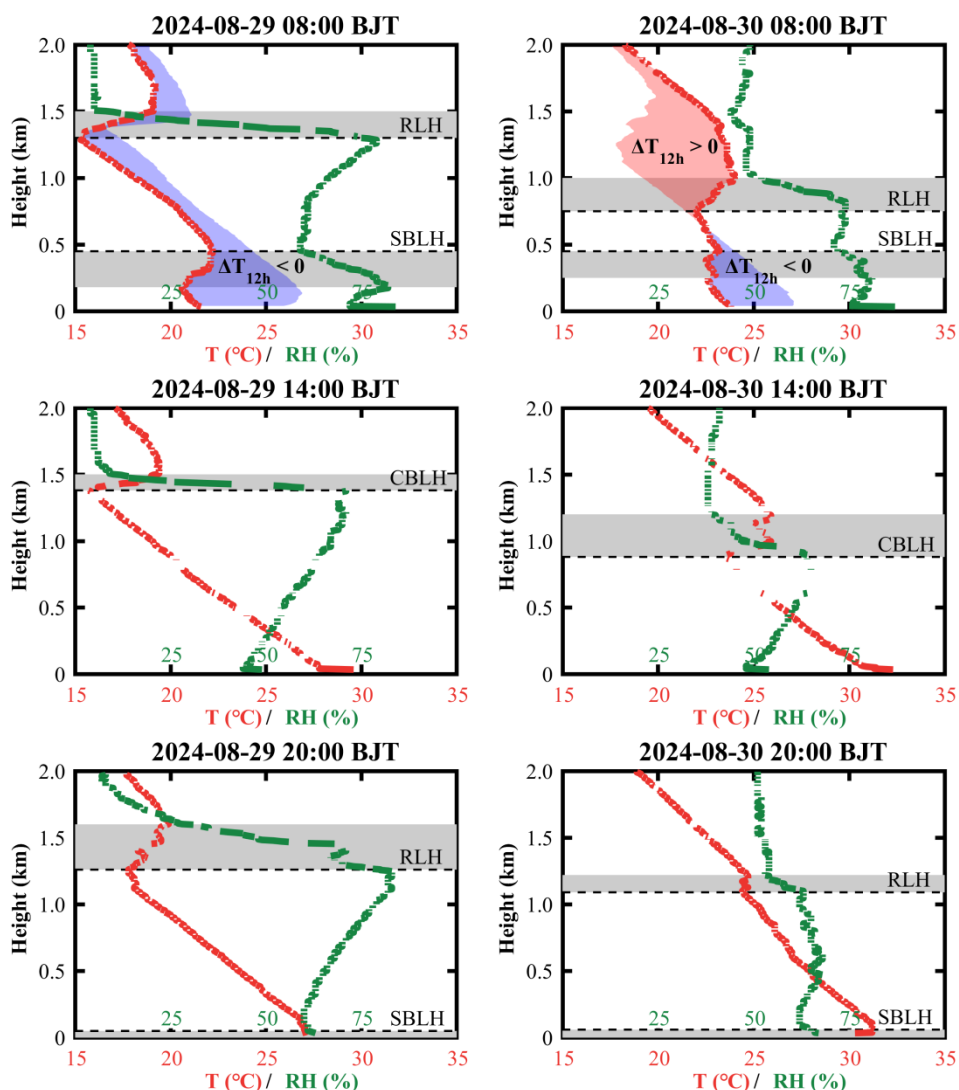
211 So, what underlying mechanism was responsible for this phenomenon?



212  
213 **Figure 4.** Weather charts at 500 hPa and sea-level pressure over the East Asia at 08:00 BJT on 29 and 30 August,  
214 2024. Shaded areas denote the cloud cover. The location of Beijing is marked by a red star.

215  
216 To address the question above, we examined the radiosonde profiles and derived boundary layer heights at the  
217 GXT station (Fig. 5). The results indicate that the CBLH and RLH on 30 August (750, 880, and 1090 m at 08:00,  
218 14:00, and 20:00 BJT, respectively) were significantly lower than those on 29 August (1300, 1380, and 1260 m at the  
219 same times), despite the SBLH showing no significant difference. The CBLH defines the available volume that the  
220 pollutants emitted/produced near the surface can occupy, directly affecting their surface concentration and air quality  
221 (Tang et al., 2016). Evidently, the significant decline in CBLH contributes to the surface O<sub>3</sub> enhancements in urban  
222 Beijing on 30 August. Notably, the two-day CBLH difference originated from a sharp drop (more than 500 m) in  
223 RLH between 20:00 BJT on 29 August and 08:00 BJT on 30 August. Comparing radiosonde profiles from these two  
224 time points revealed abnormal drying and warming in the residual layer, with a maximum temperature increase of up  
225 to 5.8°C at 1250 m, contrasting sharply with the normal cooling observed the previous night. The base height of this  
226 warming layer coincided precisely with the RLH observed at 08:00 BJT on 30 August, indicating that the warming  
227 process was responsible for the overnight RLH drop and thereby contributed to the subsequent daytime O<sub>3</sub> pollution  
228 exacerbation. Furthermore, the nocturnal residual layer warming inevitably contributes to higher daytime air  
229 temperatures. As observed, the afternoon boundary layer temperature on 30 August showed a significant increase  
230 compared to the previous afternoon, and this higher temperature further promotes photochemical O<sub>3</sub> production by  
231 accelerating photochemical reaction rates and enhancing emissions of volatile organic compounds and soil nitric  
232 oxide (Gu et al., 2020; Wu et al., 2024). Thus, in addition to promoting daytime O<sub>3</sub> accumulation by reducing the  
233 boundary layer height, residual layer warming also enhances daytime photochemical O<sub>3</sub> production. Moreover, these  
234 changes in boundary layer thermal properties can facilitate O<sub>3</sub> accumulation by lowering O<sub>3</sub> loss. For instance, the

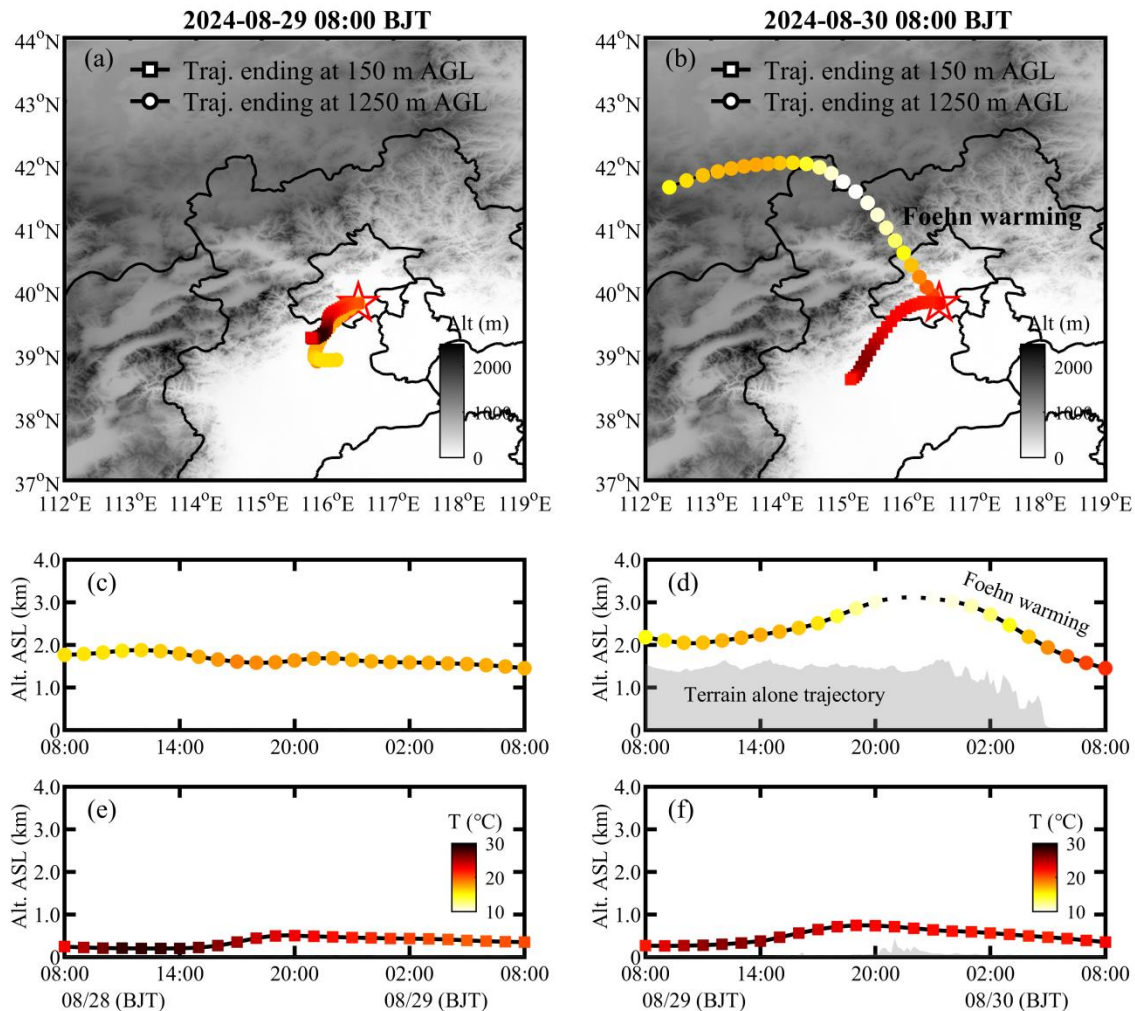
235 lowered CBLH can reduce the transport of PAN (peroxyacetyl nitrate, a NO<sub>x</sub> reservoir in the upper atmosphere) into  
 236 urban Beijing (a NO<sub>x</sub>-saturated zone), which may suppress O<sub>3</sub> loss from NO titration and independently contribute  
 237 to the observed O<sub>3</sub> increases (Flowerday and Hansen, 2026). The remaining question is: what caused the abnormal  
 238 warming of the nocturnal residual layer under the background of a cold front intrusion?



239 **Figure 5.** Radiosonde-based temperature (T, red lines) and relative humidity (RH, green lines) profiles at the GXT  
 240 station. Gray shaded areas represent the heights of temperature inversion layers. Dashed lines denote the afternoon  
 241 convective boundary layer height (CBLH), and dot lines denote the nocturnal stable boundary layer height (SBLH).  
 242 Colorful shaded areas highlight the overnight temperature changes, with increase marked in red and decrease in blue.  
 243 Note: at 08:00 BJT (morning transition), emerging solar radiation collapses the near-surface SBL; thus, the SBLH at  
 244 this time is determined at the top of the residual underlying temperature inversion.  
 245

246  
 247 Using the HYSPLIT model, we traced the 24-hour origin and characteristics of the air mass at the overnight  
 248 maximum warming height (1250 m) observed at 08:00 BJT on 30 August (Fig. 6b and d). For comparison, we also  
 249 calculated backward trajectories for the near-surface (150 m) airflow at the same time (Fig. 6b and f), as well as  
 250 airflows at the same heights and time on the previous day (Fig. 6a, c, and e). The results show that the airflows at  
 251 1250 m and 150 m on 29 August, as well as at 150 m on 30 August, all originated from the southern NCP region with  
 252 no significant change in trajectory height. In contrast, the air mass at the maximum warming height on 30 August

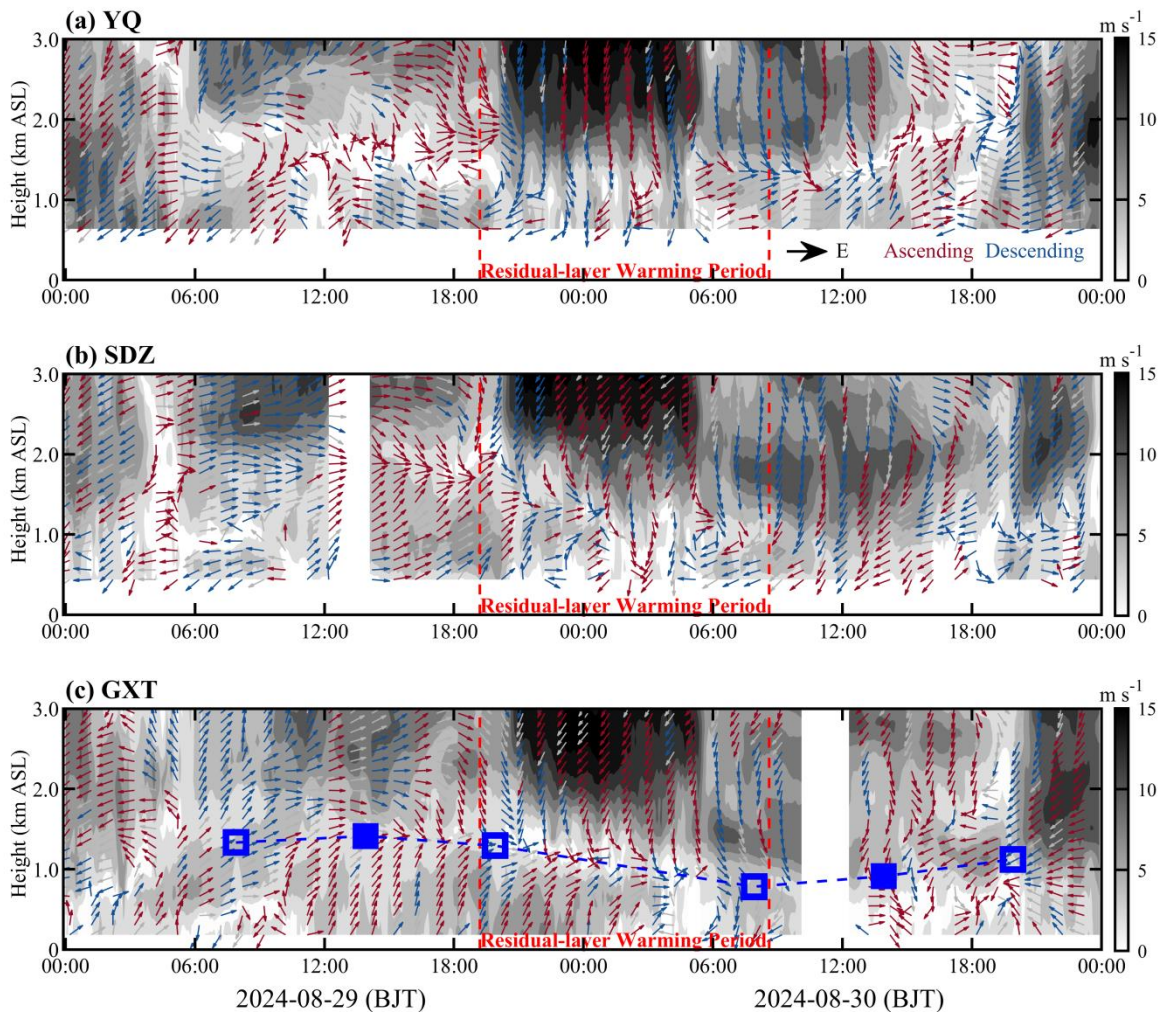
253 originated from the Mongolian Plateau. It moved eastward to the northern side of the Yanshan Mountains, turned  
 254 southeastward to cross the mountains, and finally arrived in Beijing. During this transport, the airflow first ascended  
 255 about 1000 m and then descended about 1500 m, accompanied by a temperature change of cooling (7.6°C) followed  
 256 by warming (11.4°C). These changes in trajectory height and temperature exhibit very pronounced foehn warming  
 257 characteristics (Elvidge and Renfrew, 2016). Previous studies have reported several cases of shallow foehn-induced  
 258 nocturnal surface warming in Beijing (Li et al., 2026; Luo et al., 2020). Our case differs significantly because it  
 259 involves elevated air masses and shows no warming in the surface layer. To confirm this, we examined hourly  
 260 temperature variations from 20:00 BJT on 29 August to 08:00 BJT on 30 August at 20 surface meteorological stations  
 261 in Beijing (Fig. S3), as well as at 15 levels on a 325 m high meteorological tower (Fig. S4). The results revealed that,  
 262 except for the high-altitude Foyeding station (1224.9 m), no temperature surges ( $\Delta T_{1h} > 1^\circ\text{C}$ ) were observed before  
 263 sunrise (around 06:00 BJT) at the other stations. This implies no detectable foehn warming signature from standard  
 264 mountain-leeside surface observations (Li et al., 2025), despite the strong foehn signature in the residual layer.  
 265 Therefore, we identify this case as the first observation of a novel type of foehn phenomenon in Beijing: elevated  
 266 foehn in the residual layer.



267  
 268 **Figure 6.** 24-h backward trajectories ending at 150 m (squares) and 1250 m (dots) above ground level (AGL) over  
 269 the GXT station, at 08:00 BJT of (a) 29 and (b) 30 August. The 1250 m level corresponds to the maximum overnight  
 270 warming height at 08:00 BJT on 30 August (see Fig. 5). Panels (c-f) show the height and temperature changes of 24-  
 271 h backward trajectories at 150 and 1250 m. All temperature changes share the same colorbar, including those in (a)  
 272 and (b).

273

274 To illustrate the dynamical conditions during the elevated foehn-induced residual layer warming, Figure 7 presents  
275 the radar wind profiles at the YQ, SDZ, and GXT stations from 29 to 30 August. Prior to the warming, southerly  
276 winds prevailed in the boundary layer (southwesterly at SDZ and GXT; southeasterly at YQ), while lower free-  
277 tropospheric winds gradually shifted from southwesterly to northwesterly. After sunset on 29 August, the cold front  
278 intrusion induced strong northeasterly winds in the lower free troposphere at all stations. These northeasterly winds  
279 aloft first descended into the boundary layer at YQ, followed by SDZ. In contrast, GXT maintained southwesterly  
280 boundary-layer winds until later in the night, forming a distinct northwesterly wind shear zone aloft. During this  
281 process, the height of the northwesterly wind shear corresponded well with the sounding-derived RLH at GXT, and  
282 the northwesterly winds matched the HYSPLIT backward trajectories ending at GXT (Fig. 6b). Combining the  
283 HYSPLIT results, these features strongly support the mechanism of an elevated northwesterly foehn during the  
284 residual layer warming period. The elevated foehn appears to have occurred within a shallow wind shear zone, similar  
285 to the elevated foehn scenario reported in winter Urumqi by Li et al. (2015). After the residual layer warming,  
286 northeasterlies prevailed in the boundary layer at SDZ and southwesterlies at YQ, whereas GXT showed highly  
287 variable winds with weak speeds—likely due to convergence between the emerging northwesterly foehn and the  
288 prevailing southwesterly flows. This weak-wind stagnant condition suppressed the horizontal dispersion of air  
289 pollutants. Operating in conjunction with the inhibited vertical dispersion (from a lower boundary layer height) and  
290 accelerated photochemical production (due to higher temperatures), this post-foehn convergent stagnation represent  
291 a third contributing factor to the severe daytime O<sub>3</sub> pollution observed in urban Beijing on 30 August.

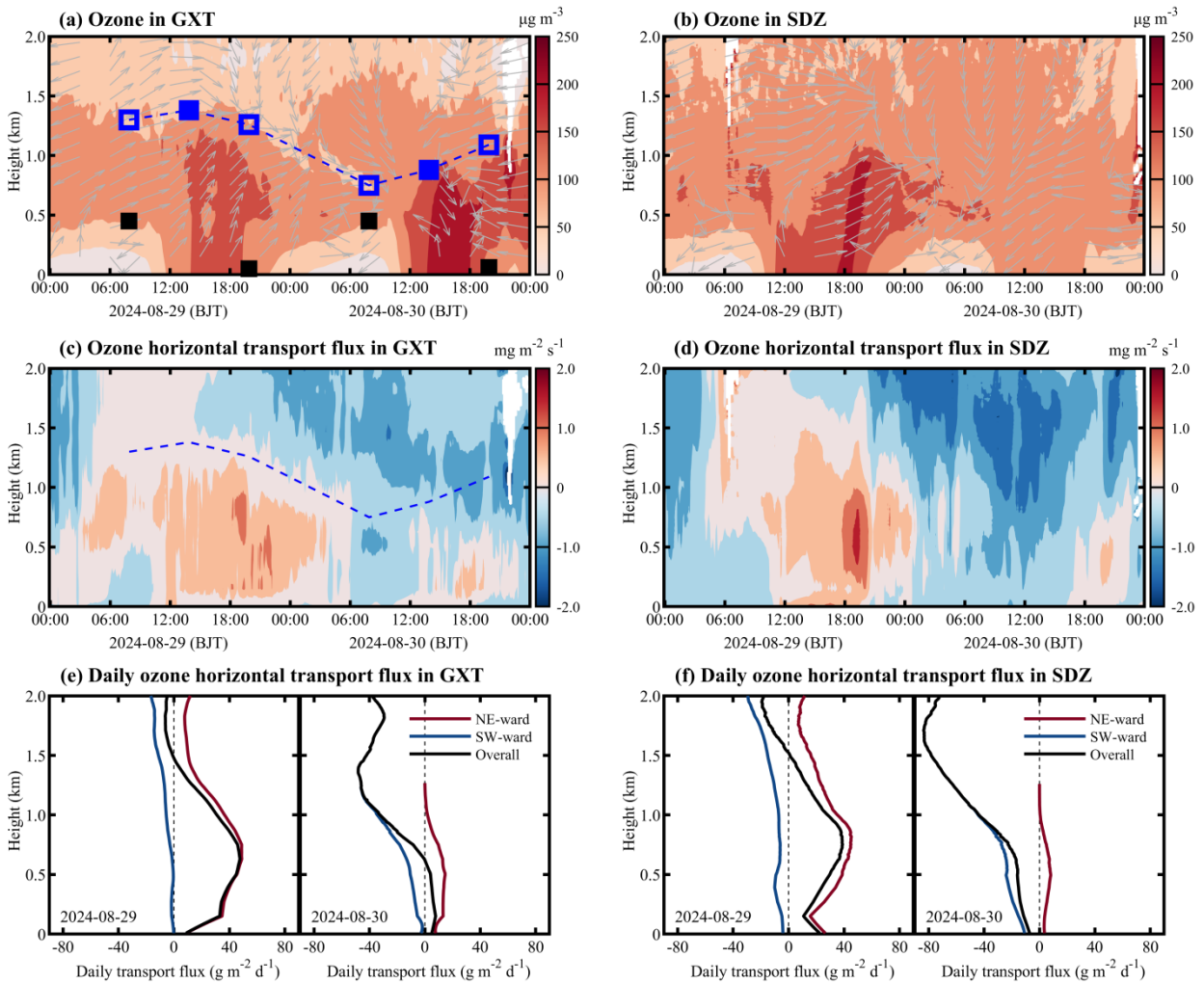


292

293 **Figure 7.** Radar-based wind profiles at the (a) YQ, (b) SDZ, and (c) GXT stations before, during, and after the  
 294 elevated foehn-induced residual layer warming. Shaded areas represent horizontal wind speed; arrows denote  
 295 horizontal wind direction (red indicates ascending motion, blue indicated descending motion). In (c), blue squares  
 296 denote the convective boundary layer height (solid) or residual layer height (hollow); blue dashed line indicates the  
 297 evolution of the convective boundary layer and residual layer heights.  
 298

### 299 3.1.3. Three-dimensional evolution of O<sub>3</sub> before, during, and after elevated foehn

300 The coordinated O<sub>3</sub> lidar observations at the urban (GXT) and rural (SDZ) stations provided a unique opportunity  
 301 to elucidate the three-dimensional evolution of boundary-layer O<sub>3</sub> in response to elevated foehn. By integrating data  
 302 from meteorological radiosondes and radar wind profilers, we investigated how sudden changes in boundary layer  
 303 thermal and dynamical structure induced by elevated foehn affected O<sub>3</sub> evolution and quantified the differences in  
 304 boundary layer O<sub>3</sub> transport fluxes between the pre- and post-foehn days (Fig. 8).



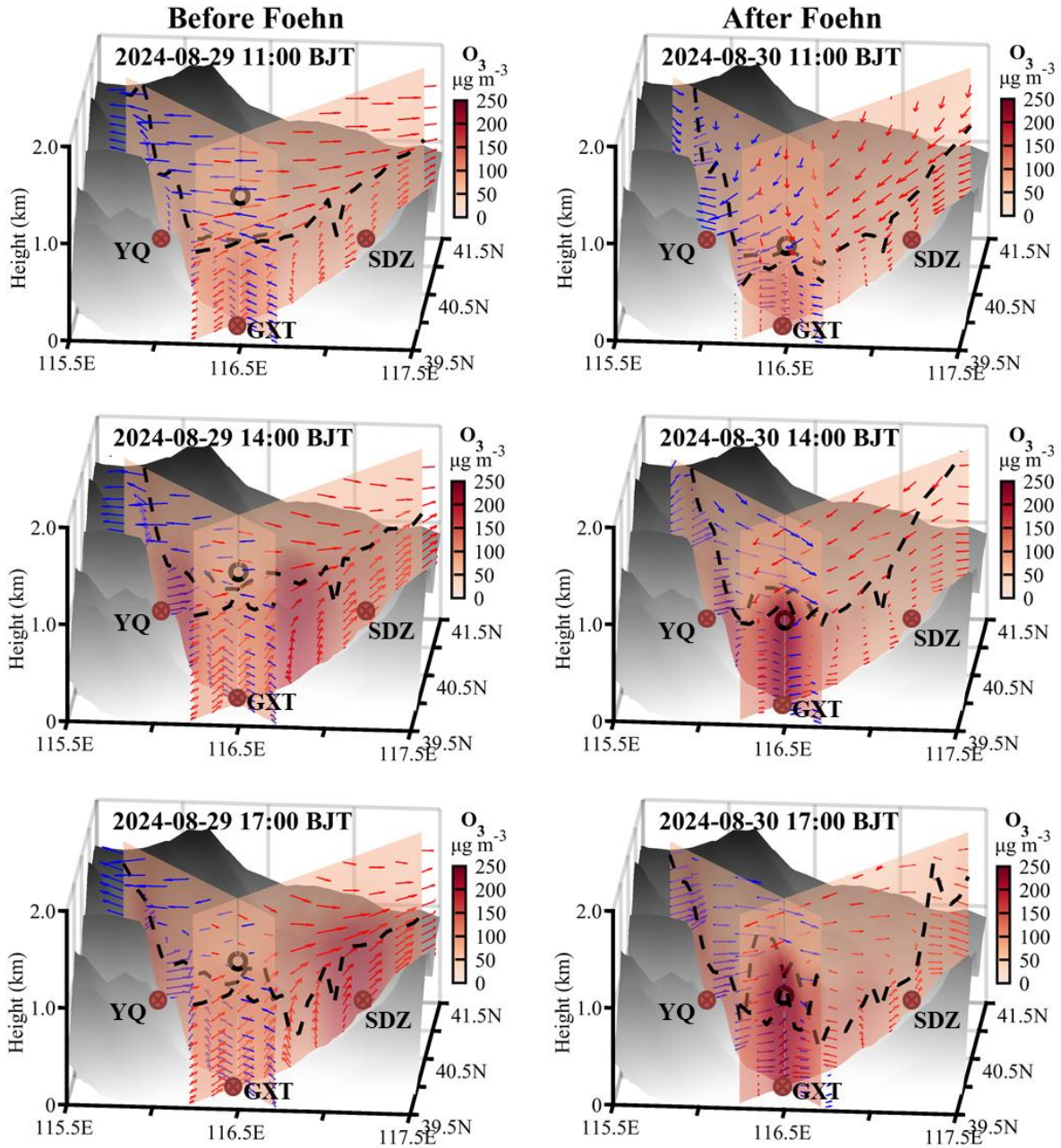
305 **Figure 8.** Vertical O<sub>3</sub> concentrations, wind direction, and O<sub>3</sub> transport flux at the GXT and SDZ stations. In (a),  
 306 squares denote the boundary layer heights determined from radiosonde profiles (black for SBLH, blue for  
 307 CBLH/RLH). The blue dashed line in (a) and (c) indicates the evolution of CBL and RL heights. In (c) and (d),  
 308 positive (negative) horizontal transport flux indicates northeastward (southwestward) transport in the direction from  
 309 GXT to SDZ. Panels (e) and (f) show the daily integrated O<sub>3</sub> transport flux at the GXT and SDZ stations on 29  
 310 and 30 August, respectively.  
 311

312

313 As shown in Fig. 8a, the boundary layer thermal structure critically shaped O<sub>3</sub> vertical distribution in urban Beijing:  
314 a steep gradient in the SBL, an O<sub>3</sub> reservoir in the RL, and relatively uniform mixing in the CBL. The elevated foehn-  
315 induced residual layer warming on the night of 29–30 August led to a significant reduction in the boundary layer  
316 height on 30 August, substantially compressing the vertical space for daytime O<sub>3</sub> mixing. Combined with enhanced  
317 photochemical O<sub>3</sub> production (due to higher temperatures) and weakened horizontal dispersion (due to lower post-  
318 foehn wind speeds,) these factors collectively contributed to a marked increase in afternoon boundary layer O<sub>3</sub>  
319 concentrations in urban Beijing on 30 August (200–250 μg m<sup>-3</sup>) compared to the previous day (~150 μg m<sup>-3</sup>). We  
320 also observed that the elevated foehn was accompanied by downward transport of free-tropospheric O<sub>3</sub> (Fig. 8a).  
321 However, due to the presence of a strong capping inversion acting as a transport barrier (Fig. 5), this descending free-  
322 tropospheric O<sub>3</sub> was unlikely to have significantly intruded into the boundary layer.

323  
324 The urban-rural coordinated lidar observations clearly reveal a dynamically driven shift in spatial heterogeneity  
325 before and after the elevated foehn. On 29 August (pre-foehn), prevailing southwesterly flows facilitated the  
326 northeastward transport of the urban O<sub>3</sub> plume. The lidars recorded higher O<sub>3</sub> concentrations at the downwind rural  
327 SDZ station than at the urban GXT station (Fig. 8a and b). The peak O<sub>3</sub> occurrence at SDZ was delayed by 1–3 hours  
328 relative to GXT, consistent with advective transport. The calculated horizontal O<sub>3</sub> transport flux was predominantly  
329 northeastward in the boundary layer at both stations throughout the day, with stronger fluxes in the upper boundary  
330 layer. The instantaneous maximum flux at SDZ exceeded 2.0 mg m<sup>-3</sup> s<sup>-1</sup>, significantly higher than at GXT (Fig. 8c  
331 and d). In stark contrast, the post-foehn convergence stagnation on 30 August suppressed advective transport and  
332 promoted local O<sub>3</sub> accumulation in urban Beijing. Consequently, afternoon boundary layer O<sub>3</sub> concentrations at GXT  
333 reached notably high levels (200–250 μg m<sup>-3</sup>), while concentrations at SDZ dropped to low values (~100 μg m<sup>-3</sup>).  
334 Despite this spatial contrast, the boundary layer O<sub>3</sub> transport flux at both stations was markedly low compared to the  
335 previous day (Fig. 8c, d, e, and f), underscoring a shift in the dominant pollution mechanism from urban plume  
336 transport to urban pollution accumulation.

337  
338 We examined the WRF-Chem output to gain further insight into the vertical O<sub>3</sub> structure over Beijing before and  
339 after the elevated foehn. As shown in Fig. 9, although the WRF-Chem model exhibited some deviations in simulating  
340 the boundary layer height, it successfully reproduced the pre-foehn northeastward transport of the urban O<sub>3</sub> plume  
341 on 29 August, as well as the post-foehn stagnation-driven local O<sub>3</sub> accumulation in the urban Beijing on 30 August.  
342 On 29 August, the O<sub>3</sub> pollution initially built up in the urban area (e.g., near GXT) by 11:00 BJT. By 14:00 BJT, the  
343 high-O<sub>3</sub> zone had shifted to the northern suburbs, and by 17:00 BJT, it had been transported to the rural areas in the  
344 northeast (e.g., near SDZ). In contrast, on 30 August, the relatively higher O<sub>3</sub> concentrations over Beijing were  
345 consistently confined in the urban area, with no significant spatial shift. These simulation results aligned well with  
346 the lidar observations. Furthermore, the WRF-Chem model reproduced the vertical wind patterns observed at GXT,  
347 SDZ, and YQ (Fig. 7), thereby better illustrating the vertical structure of the foehn flow during its decaying stage on  
348 30 August via wind cross-sections. The foehn simulations show that while the near-surface component—shallow  
349 foehn—was blocked by prevailing southerly winds within the boundary layer, leading to convergence and airflow  
350 stagnation over urban Beijing, its upper-layer branch—elevated foehn—passed directly over the urban area  
351 unimpeded, resulting in persistent warming that suppressed the daytime convective boundary layer development until  
352 the foehn decayed around 14:00 BJT. These features are evident in both the GXT-YQ cross-section (parallel to the  
353 elevated northwesterly foehn) and the GXT-SDZ cross-section (perpendicular to the elevated northwesterly foehn).  
354 The configuration of an unimpeded elevated foehn and a blocked shallow foehn effectively explains the accumulation  
355 of higher O<sub>3</sub> concentrations in the urban boundary layer of Beijing on 30 August.



356

357 **Figure 9.** Cross-sections of simulated  $O_3$  concentrations along the line across the GXT and SDZ stations and the line  
 358 across GXT and YQ stations on 29 and 30 August. Dashed black lines denote the simulated boundary layer height,  
 359 and arrows show the composite of simulated horizontal wind speed ( $m s^{-1}$ ) and vertical wind speed ( $\times 10 m s^{-1}$ ) in the  
 360 GXT-SDZ (red arrows) and GXT-YQ (blue arrows) cross-sections. Only horizontal wind speed in the direction along  
 361 the individual cross-sections is included. The black dots denote the boundary layer height observed at GXT and the  
 362 height at 14:00 BJT is the observational value and these at 11:00 and 17:00 BJT are interpolated from two adjacent  
 363 radiosonde observations.

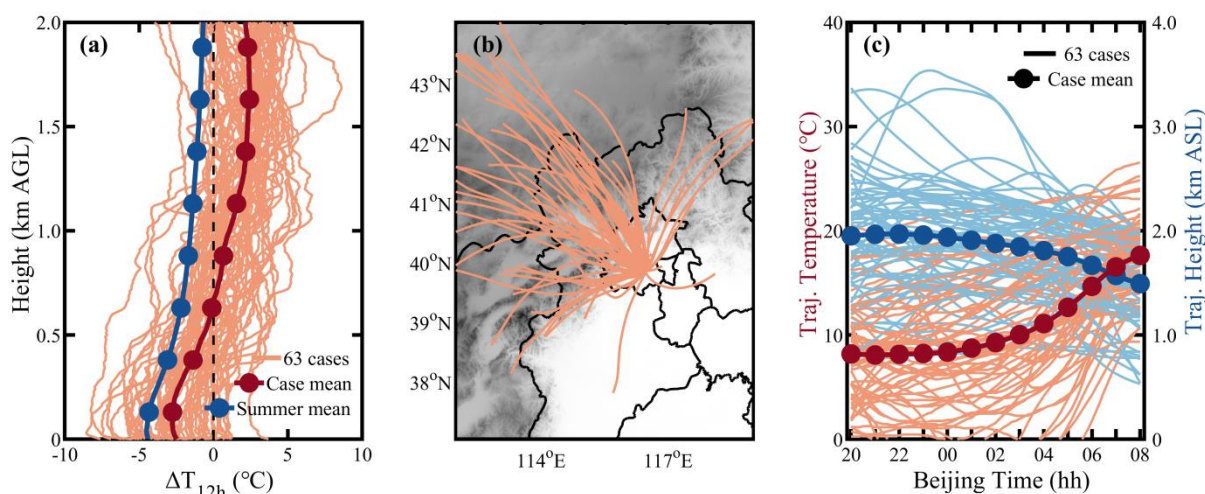
364

### 365 3.2. Climatological evaluation

366 While a case study is valuable for mechanistic understanding, the question of representativeness always arises. To  
 367 clarify whether the features identified in the case study are typical, we supplemented the case analysis with a  
 368 climatological investigation of elevated foehn and its  $O_3$  pollution effect based on long-term observations.

369

370 Based on summer radiosonde data from the GXT station during 2015-2024, we calculated overnight temperature  
 371 change ( $\Delta T_{12h}$ ) profiles for each night by differencing the temperature profiles at 20:00 BJT and 08:00 BJT the  
 372 following day. We identified a residual layer warming event when  $\Delta T_{12h} > 3^\circ\text{C}$  occurred within 500-2000 m height  
 373 range. For each event, we identified the height of maximum warming and used it as the endpoint for backward  
 374 trajectory calculations. Statistical results show that among the 920 valid summer observation days from 2015 to 2024,  
 375 a total of 63 residual layer warming cases were identified, accounting for 6.85% of summer night. Figure 10 illustrates  
 376 the  $\Delta T_{12h}$  profiles, backward trajectories, and trajectory height/temperature changes for these events. While warming  
 377 heights vary widely across different events, the composite  $\Delta T_{12h}$  profile highlights warming above  $\sim 650$  m,  
 378 contrasting sharply with the summer mean profile showing nocturnal cooling throughout the layer. The backward  
 379 trajectories of these warming air masses show that most originated from high-altitude regions to the west or north.  
 380 After crossing the Yanshan or Taihang Mountains, these airflows arrived in Beijing, with their trajectories descending  
 381 on average by 500 m and their temperature rising rapidly by an average of  $10^\circ\text{C}$ , exhibiting clear foehn characteristics.  
 382 Applying the elevated foehn criteria from Sect. 2.2, 54 of the 63 warming cases (85.7%) can be attributed to elevated  
 383 foehn. These results confirm that elevated foehn is the primary cause of nocturnal residual layer warming in Beijing.

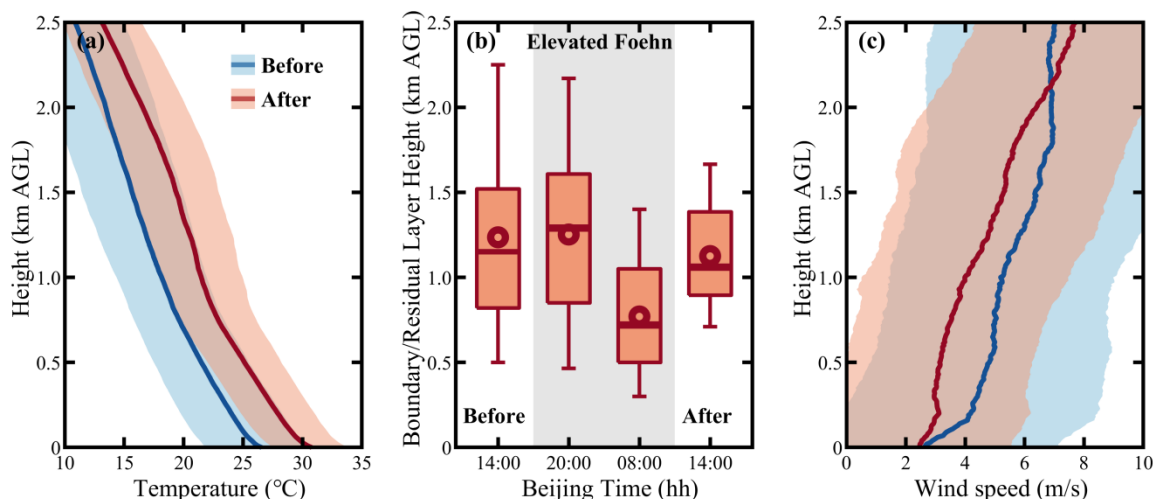


384

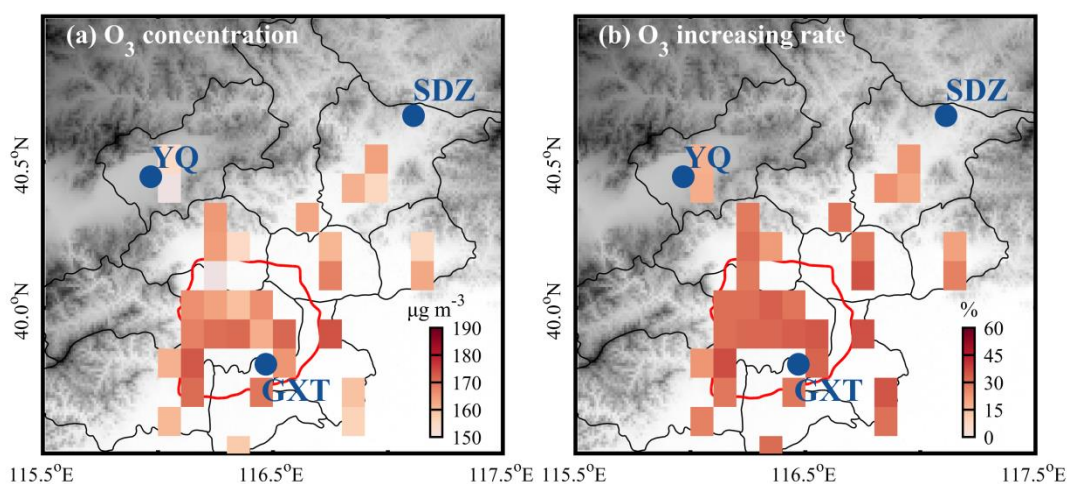
385 **Figure 10.** (a) Overnight temperature change ( $\Delta T_{12h}$ ) profiles from 20:00 BJT to next-day 08:00 BJT, (b) overnight  
 386 airflow backward trajectories ending at the maximum warming height, and (c) overnight trajectory height and  
 387 temperature changes for the 63 identified residual layer warming events.

388

389 Previous case analysis indicated that elevated foehn exacerbates next-day  $\text{O}_3$  pollution through three pathways:  
 390 increasing boundary layer temperature (enhancing photochemistry), reducing boundary layer height (inhibiting  
 391 vertical diffusion), and weakening boundary layer winds (suppressing horizontal dispersion). Composite analyses of  
 392 all 54 elevated foehn events (Fig. 11) strongly support the prevalence of these mechanisms. On average, post-foehn  
 393 afternoon boundary layer temperature was more than  $3^\circ\text{C}$  higher than pre-foehn conditions. The elevated foehn-  
 394 induced residual layer warming directly led to an average RLH reduction of 480 m, and the subsequent afternoon  
 395 CBLH was, on average, 110 m lower. Post-foehn afternoon boundary layer wind speed decreased by more than  $1.0$   
 396  $\text{m s}^{-1}$  on average. Overall, these meteorological changes consistently favor local  $\text{O}_3$  production and accumulation. As  
 397 a result, approximately 87% of elevated foehn events were followed by worsened  $\text{O}_3$  pollution. Post-foehn  $\text{MDA8O}_3$   
 398 concentrations across Beijing increased by an average of 20–60% (varying by site) compared to the preceding day  
 399 (Fig. 12b). Within the main urban zone (inside the 6th Ring Road), the  $\text{MDA8O}_3$  increase generally exceeded 45%  
 400 (Fig. 12b), with concentrations commonly surpassing the national air quality standard of  $160 \mu\text{g m}^{-3}$  (Fig. 12a).



401  
 402 **Figure 11.** Composite of (a) afternoon boundary layer temperature profiles, (b) boundary/residual layer height, and  
 403 (c) afternoon boundary layer wind speed profiles before, during, and after 54 identified elevated foehn events in  
 404 Beijing. In (a) and (c), solid lines denote the mean profiles and shaded areas represent the standard deviation. In (b),  
 405 box-and-whisker plots show the 5th, 25th, 50th, 75th, and 95th percentiles; dots represent the means.



406  
 407 **Figure 12.** Composite of (a) daily maximum 8-h  $O_3$  concentrations following elevated foehn in Beijing, and (b) their  
 408 average percentage increase compared to preceding days. Note: site data are resampled and shown on a  $0.1^\circ \times 0.1^\circ$   
 409 grid, accounting for the relocation of some sites around 2021.

410  
 411 **4. Discussion**

412 Traditionally, nocturnal warming has been considered rare. Previous studies have observed occasional nighttime  
 413 surface warming in leeward plains or valleys due to foehn effects (Luo et al., 2020; Ma et al., 2015). This study, by  
 414 creatively integrating radiosonde data, reveals for the first time the frequent occurrence of pronounced nocturnal  
 415 residual layer warming in summer Beijing. The primary driver is identified as elevated foehn—an upper-layer  
 416 phenomenon previously missed by near-surface observations. Theoretically, unlike near-surface warming from  
 417 shallow foehn (which enhances boundary layer instability), residual layer warming from elevated foehn reinforces  
 418 static stability (Stull, 1988). Our observations show that the elevated foehn-induced warming substantially lowers the  
 419 boundary layer capping inversion (i.e., RLH), thereby inhibiting the development of the next day's convective  
 420 boundary layer. While Pal and Lee (2019) highlighted that mountain air mass advection can lead to boundary layer

421 overrunning over downwind plains, our results demonstrate that under elevated foehn, mountain-sourced air masses  
422 can instead act to lower the downwind boundary layer height through foehn warming.

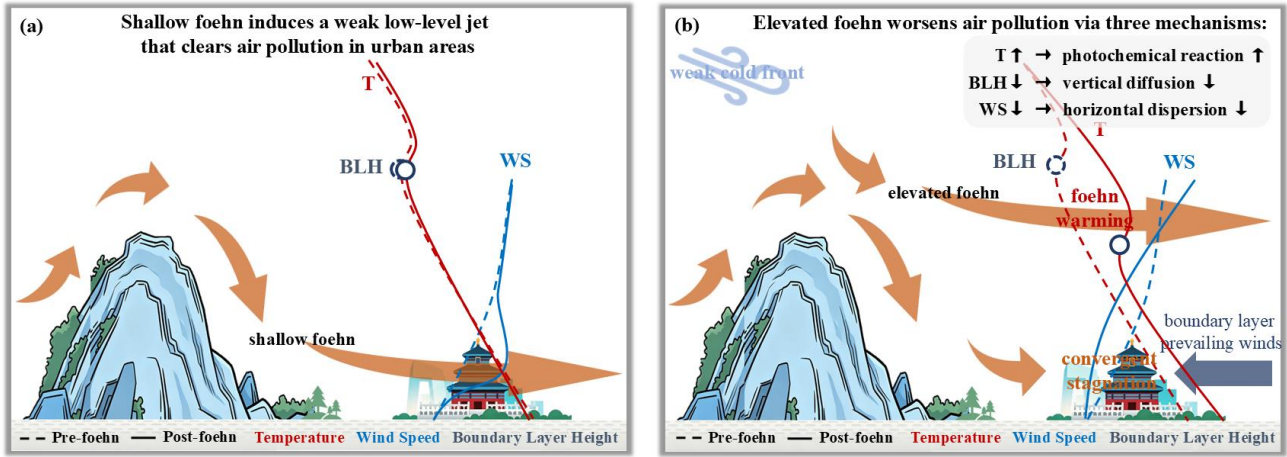
423

424 The elevated foehn process in summer Beijing shows both similarities and differences with that in winter Urumqi  
425 (Li et al., 2015). The similarity lies mainly in the three-layer flow structure that causes similar "sandwich" foehn  
426 warming within a middle wind shear layer. The key difference lies in the post-foehn boundary layer convergence  
427 mechanism. In winter Urumqi, a downslope wind and hydraulic jump occur simultaneously on the northern leeside  
428 of the Tianshan Mountains after the foehn encounters a cold air pool in the southern suburbs, generating convergence  
429 between the cold pool and the shallow downslope wind (Li et al., 2015). In contrast, no such cold air pool exists in  
430 summer Beijing. Here, the post-foehn convergence instead results from the confrontation between the emerging  
431 northwestern foehn winds and the prevailing southwestern winds within the boundary layer. The relatively strong  
432 boundary-layer southwesterly winds appear to be a necessary prerequisite for the occurrence of elevated foehn in  
433 summer Beijing, as they inhibit the intrusion of shallow foehn toward plain areas and, in turn, force the foehn to  
434 develop upward. In other words, the relatively strong boundary-layer southwesterly winds in summer Beijing likely  
435 play a role similar to that of the cold air pool in winter Urumqi in lifting the foehn to form an elevated foehn.

436

437

438 Our results reveal that 86.9% of the identified elevated foehn events were followed by O<sub>3</sub> pollution exacerbation  
439 in summer Beijing. Post-foehn MDA8O<sub>3</sub> concentrations increased more than 30% on average, exceeding the national  
440 pollution threshold at most monitoring sites. In a previous study, Li et al. (2025) explored connections between  
441 ground-based (shallow) foehn and PM<sub>2.5</sub> pollution in Beijing, finding that 60.4 % of cases corresponded to pollution  
442 mitigation and only 39.6% to exacerbation. Given that direct comparability is limited due to differences in pollutant  
443 (PM<sub>2.5</sub> vs. O<sub>3</sub>), season (annual vs. summer), and foehn type (shallow vs. elevated), we acquired the summertime  
444 shallow foehn dates identified in Li et al. (2025) and conducted additional statistics of air pollution for summertime  
445 shallow foehn events (Table S1). The statistics indicated that elevated foehn corresponds to a markedly higher  
446 probability (86.9%) of post-foehn O<sub>3</sub> pollution exacerbation compared to shallow foehn (55.2%). Similar results are  
447 found for PM<sub>2.5</sub> pollution (69.8% vs. 55.2%). These results clearly indicate that elevated foehn exhibits a more  
448 deterministic pollution-worsened effect than shallow foehn. Furthermore, we examined the changes in boundary layer  
449 structure before and after summertime shallow foehn events (Fig. S5). The results revealed no significant changes in  
450 boundary layer temperature or boundary layer height. However, shallow foehn tends to induce a weak low-level jet,  
451 which can clear air pollution in urban areas and thereby inhibit pollution exacerbation. In light of the above  
452 comparison, we summarized a conceptual diagram in Fig. 13 to illustrate the distinct pollution mechanisms associated  
453 with shallow versus elevated foehn. Overall, elevated foehn can serve as a more reliable meteorological precursor for  
454 O<sub>3</sub> pollution warnings in summer Beijing. Since elevated foehn can be directly identified from routine radiosonde  
455 observations (Sect. 2.2), its application as a precursor for summer O<sub>3</sub> forecasting can be both highly convenient and  
456 timely.



457

458 **Figure 13.** Conceptual diagram illustrating the distinct pollution mechanisms associated with shallow versus elevated  
 459 foehn.

460

461 **5. Conclusion**

462 This study systematically investigated the formation process of elevated foehn winds and their mechanisms for  
 463 exacerbating surface O<sub>3</sub> pollution in summer Beijing through a combined case analysis and climatological evaluation.  
 464 The main conclusions are as follows:

- 465 1、 First observational confirmation of elevated foehn events in summer Beijing. Utilizing high-resolution  
 466 radiosonde observations, this study identified a novel phenomenon distinct from traditional near-surface foehn.  
 467 It manifests as abnormal nocturnal warming ( $\Delta T_{12h} > 3^{\circ}\text{C}$ ) within the elevated residual layer (approximately 500–  
 468 2000 m AGL), with no significant warming signal at the surface. Lagrangian back-trajectory analysis confirms  
 469 that the warming air masses originate from the northwestern or northern plateaus, undergoing descent and  
 470 warming after crossing the Yanshan or Taihang Mountains, exhibiting classic foehn characteristics. These  
 471 elevated foehn events account for 5.87% of summer nights and are identified as the primary driver (85.7% of  
 472 identified cases) of nocturnal residual layer warming in Beijing.
- 473 2、 Clarification of the triple synergistic mechanisms through which elevated foehn exacerbates next-day O<sub>3</sub>  
 474 pollution. Thermodynamic Effect I: Increasing boundary layer temperature to enhance photochemical production.  
 475 Nocturnal residual layer warming directly leads to a significantly higher daytime boundary layer temperature  
 476 (average increase  $> 3^{\circ}\text{C}$ ), accelerating the photochemical reaction rates of precursors. Thermodynamic Effect II:  
 477 Lowering the boundary layer height to suppress vertical diffusion. The residual layer warming reinforces  
 478 atmospheric stability, causing the capping inversion base (i.e., the residual layer height) to drop by an average of  
 479  $\sim 480$  m and the subsequent afternoon convective boundary layer height to decrease by  $\sim 110$  m. This substantially  
 480 compresses the vertical mixing volume for pollutants. Dynamic Effect: Inducing boundary-layer convergent  
 481 stagnation to weaken horizontal transport. The intruding northwesterly elevated foehn flow confronts the  
 482 prevailing southwesterlies within the boundary layer, forming a convergence zone. This leads to a marked  
 483 reduction in wind speed (average decrease  $> 1.0 \text{ m s}^{-1}$ ), severely hindering the horizontal advective dispersion of  
 484 pollutants.
- 485 3、 Decade-long climatological evaluation confirms the highly deterministic and prevalent exacerbating effect of  
 486 elevated foehn on summer O<sub>3</sub> pollution. Composite analysis of 54 identified elevated foehn events from 2015–  
 487 2024 robustly supports the proposed mechanisms. Statistics show that 87% of elevated foehn events were  
 488 followed by worsened O<sub>3</sub> pollution the next day. The city-wide MDA<sub>8O<sub>3</sub></sub> concentration increased by 20–60% on  
 489 average compared to the preceding day, with increases in the main urban area typically exceeding 45%. Post-

490 foehn MDA8O<sub>3</sub> concentrations commonly surpassed the national ambient air quality standard (160 μg m<sup>-3</sup>). This  
491 stands in sharp contrast to additional statistics based on near-surface observations, which associate shallow foehn  
492 primarily with no significant pollution changes, highlighting the fundamental difference in pollution potential  
493 between shallow and elevated foehn.  
494

495 In summary, this study identifies elevated foehn as a significant and previously overlooked meteorological forcing  
496 factor for summer O<sub>3</sub> pollution in Beijing. Its synergistic "warming-lowering-stagnating" effects lead to a highly  
497 deterministic pollution exacerbation. Given that elevated foehn can be directly identified using routine radiosonde  
498 data, we propose its utility as a reliable and efficient meteorological precursor for O<sub>3</sub> pollution forecasting and  
499 warning in Beijing and other cities with similar topography. This provides a new scientific basis for the precise  
500 prevention and control of air pollution. Future research should focus on quantifying the contribution of elevated foehn  
501 to O<sub>3</sub> generation under different synoptic backgrounds and exploring its coupling with regional transport and  
502 chemical processes.  
503

504 To date, numerous circulation classification-based studies have highlighted the importance of synoptic-scale  
505 weather on regional O<sub>3</sub> pollution in the NCP region (Dong et al., 2020; Han et al., 2020; Liao et al., 2024; Liu et al.,  
506 2019). However, day-to-day circulation classifications actually overlook sub-daily meteorological processes, such as  
507 the nocturnal elevated foehn identified in this study. A very recent study (Xu et al., 2026) indicated that ground-based  
508 foehns on the eastern Taihang Mountains preferentially occur under stable atmospheric stratification, with a surface  
509 high over the windward side and a low over the leeward side, together with an upper-level cold trough at 500 hPa  
510 and pronounced subsidence at 850 hPa on the leeward side on the eastern foothills of the Taihang Mountains.  
511 However, this study did not extend its findings to the field of air pollution, nor did it clarify whether the  
512 aforementioned synoptic conditions are also conducive to the occurrence of elevated foehn. Overall, a better coupling  
513 of synoptic-scale circulation patterns and local-scale elevated foehn processes will further deepen our understanding  
514 of meteorological mechanisms underlying O<sub>3</sub> pollution.  
515

#### 516 ***Code and data availability.***

517 Hourly surface ozone data, except for those from the SDZ station, were obtained from the China National  
518 Environmental Centre (<http://www.cnemc.cn/en/>). The HYSPLIT model and its compatible meteorological data were  
519 sourced from the NOAA Air Resources Laboratory (<https://www.ready.noaa.gov/HYSPLIT.php>). We are not  
520 authorized to publicly release the following raw data: hourly ozone measurements at the SDZ station, radiosonde  
521 data, ozone lidar observations, wind profiler radar measurements, and numerical simulation outputs. These datasets  
522 are available from the corresponding author upon reasonable request. ~~The remote sensing observations and numerical~~  
523 ~~simulation results are available from the correspondence author upon reasonable request~~ ([zqma@ium.cn](mailto:zqma@ium.cn)).  
524

#### 525 **Author contributions**

526 Z.L. conceived the original idea, analyzed the data, and wrote the first version manuscript. J.X. conducted the WRF-  
527 Chem simulation. L.Z. operated the remote sensing equipment. C.L. performed the HYSPLIT model. Z.M. supervised  
528 the research project. All authors discussed the results and commented on the manuscript.  
529

#### 530 **Competing interests**

531 The authors declare no competing interests.  
532

#### 533 **Acknowledgements**

534 This research has been supported by the National Natural Science Foundation of China (Grant Nos. 42405115 and  
535 42307150), and the Scientific Research Project of the Beijing Meteorological Bureau (Grant No. BMBKJ202404002).  
536 We acknowledge the DeepSeek for polishing our English language. We thank the two anonymous reviewers for their  
537 comments, which have greatly improved the quality of the manuscript.  
538

## 539 **References**

- 540 Baumann, K., Maurer, H., Rau, G., Piringer, M., Pechinger, U., Prévôt, A., Furger, M., Neining, B., Pellegrini, U., 2001. The  
541 influence of south Foehn on the ozone distribution in the Alpine Rhine valley—results from the MAP field phase.  
542 *Atmospheric Environment* 35, 6379-6390.
- 543 Campana, M., Li, Y., Staehelin, J., Prevot, A.S.H., Bonasoni, P., Loetscher, H., Peter, T., 2005. The influence of south foehn  
544 on the ozone mixing ratios at the high alpine site Arosa. *Atmospheric Environment* 39, 2945-2955.
- 545 Dong, Y.M., Li, J., Guo, J.P., Jiang, Z.J., Chu, Y.Q., Chang, L., Yang, Y., Liao, H., 2020. The impact of synoptic patterns on  
546 summertime ozone pollution in the North China Plain. *Sci Total Environ* 735.
- 547 Elvidge, A.D., Renfrew, I.A., 2016. The Causes of Foehn Warming in the Lee of Mountains. *Bulletin of the American*  
548 *Meteorological Society* 97, 455-466.
- 549 Flowerday, C., Hansen, J.C., 2026. Peroxyacetyl Nitrate (PAN) in the Atmosphere: A Comprehensive Review of Chemistry,  
550 Measurements, and Chemical-Transport Implications. *Environmental Science: Atmospheres*.
- 551 Gaffin, D.M., 2002. Unexpected Warming Induced by Foehn Winds in the Lee of the Smoky Mountains. *Weather and*  
552 *Forecasting* 17, 907-915.
- 553 Gaffin, D.M., 2009. On High Winds and Foehn Warming Associated with Mountain-Wave Events in the Western Foothills  
554 of the Southern Appalachian Mountains. *Weather and Forecasting* 24, 53-75.
- 555 Grell, G.A., Peckham, S.E., Schmitz, R., McKeen, S.A., Frost, G., Skamarock, W.C., Eder, B., 2005. Fully coupled “online”  
556 chemistry within the WRF model. *Atmospheric Environment* 39, 6957-6975.
- 557 Gu, Y., Li, K., Xu, J., Liao, H., Zhou, G., 2020. Observed dependence of surface ozone on increasing temperature in Shanghai,  
558 China. *Atmospheric Environment* 221, 117108.
- 559 Guenther, A., Karl, T., Harley, P., Wiedinmyer, C., Palmer, P.I., Geron, C., 2006. Estimates of global terrestrial isoprene  
560 emissions using MEGAN (Model of Emissions of Gases and Aerosols from Nature). *Atmos. Chem. Phys.* 6, 3181-3210.
- 561 Han, H., Liu, J.E., Shu, L., Wang, T.J., Yuan, H.L., 2020. Local and synoptic meteorological influences on daily variability in  
562 summertime surface ozone in eastern China. *Atmos Chem Phys* 20, 203-222.
- 563 Kerr, R.A., 1986. Chinook Winds Resemble Water Flowing over a Rock. *Science* 231, 1244-1245.
- 564 Kirchgaessner, A., King, J.C., Anderson, P.S., 2021. The Impact of Föhn Conditions Across the Antarctic Peninsula on Local  
565 Meteorology Based on AWS Measurements. *Journal of Geophysical Research: Atmospheres* 126, e2020JD033748.
- 566 Li, J., Sun, Z., Lenschow, D.H., Zhou, M., Dou, Y., Cheng, Z., Wang, Y., Li, Q., 2020a. A foehn-induced haze front in Beijing:  
567 observations and implications. *Atmos. Chem. Phys.* 20, 15793-15809.
- 568 Li, J., Zhang, J., Bai, M., Su, J., Li, Q., Jia, X., 2025. Identification and characterization of foehn events in Beijing and their  
569 impact on air pollution episodes. *Atmos. Chem. Phys.* 25, 8683-8700.
- 570 Li, X., Xia, X., Wang, L., Cai, R., Zhao, L., Feng, Z., Ren, Q., Zhao, K., 2015. The role of foehn in the formation of heavy air  
571 pollution events in Urumqi, China. *Journal of Geophysical Research: Atmospheres* 120, 5371-5384.
- 572 Li, X., Xia, X., Zhong, S., Luo, L., Yu, X., Jia, J., Zhao, K., Li, N., Liu, Y., Ren, Q., 2020b. Shallow foehn on the northern leeside  
573 of Tianshan Mountains and its influence on atmospheric boundary layer over Urumqi, China — A climatological study.  
574 *Atmospheric Research* 240, 104940.
- 575 Li, Y., Chen, M., Miao, S., Zhang, G., Huang, Q., Zhang, S., 2026. Evaluation of three scale-aware planetary boundary layer  
576 schemes in WRF Model during Beijing 2022 Winter Olympics. *Atmospheric Research* 328, 108416.
- 577 Liao, Z., Pan, Y., Ma, P., Jia, X., Cheng, Z., Wang, Q., Dou, Y., Zhao, X., Zhang, J., Quan, J., 2023. Meteorological and chemical

578 controls on surface ozone diurnal variability in Beijing: A clustering-based perspective. *Atmospheric Environment* 295,  
579 119566.

580 Liao, Z., Sun, J., Yao, J., Liu, L., Li, H., Liu, J., Xie, J., Wu, D., Fan, S., 2018. Self-organized classification of boundary layer  
581 meteorology and associated characteristics of air quality in Beijing. *Atmos. Chem. Phys.* 18, 6771-6783.

582 Liao, Z.H., Jia, X.C., Qiu, Y.L., Quan, J.N., Pan, Y.B., Ma, P.K., Cheng, Z.G., Wang, Q.Q., 2024. Synoptic controls on warm-  
583 season O<sub>3</sub> pollution in eastern China: A focus on O<sub>3</sub>-NO<sub>x</sub>-VOC chemistry. *Atmospheric Research* 311, 107660.

584 Liu, J.D., Wang, L.L., Li, M.G., Liao, Z.H., Sun, Y., Song, T., Gao, W.K., Wang, Y.H., Li, Y., Ji, D.S., Hu, B., Kerminen, V.M., Wang,  
585 Y.S., Kulmala, M., 2019. Quantifying the impact of synoptic circulation patterns on ozone variability in northern China from  
586 April to October 2013-2017. *Atmos Chem Phys* 19, 14477-14492.

587 Liu, S., Liang, X.-Z., 2010. Observed Diurnal Cycle Climatology of Planetary Boundary Layer Height. *Journal of Climate* 23,  
588 5790-5809.

589 Luo, R., Zheng, Y., Chen, M., 2020. Mechanism of a rare night sudden intense warming event in Beijing and surrounding  
590 area. *Meteorol. Monthly (in Chinese)* 46, 478-489.

591 Ma, Y., Yang, Y., Hu, X., Gan, R., 2015. Characteristics and Mechanisms of the Sudden Warming Events in the Nocturnal  
592 Atmospheric Boundary Layer: A Case Study Using WRF. *Journal of Meteorological Research* 29, 747-763.

593 Miltenberger, A.K., Reynolds, S., Sprenger, M., 2016. Revisiting the latent heating contribution to foehn warming:  
594 Lagrangian analysis of two foehn events over the Swiss Alps. *Quarterly Journal of the Royal Meteorological Society* 142,  
595 2194-2204.

596 Ouyang, S., Deng, T., Liu, R., Chen, J., He, G., Leung, J.C.H., Wang, N., Liu, S.C., 2022. Impact of a subtropical high and a  
597 typhoon on a severe ozone pollution episode in the Pearl River Delta, China. *Atmos. Chem. Phys.* 22, 10751-10767.

598 Pal, S., Lee, T.R., 2019. Advected Air Mass Reservoirs in the Downwind of Mountains and Their Roles in Overrunning  
599 Boundary Layer Depths Over the Plains. *Geophysical Research Letters* 46, 10140-10149.

600 Seibert, P., Feldmann, H., Neininger, B., Bäuml, M., Trickl, T., 2000. South foehn and ozone in the Eastern Alps – case  
601 study and climatological aspects. *Atmospheric Environment* 34, 1379-1394.

602 Shu, L., Xie, M., Wang, T., Gao, D., Chen, P., Han, Y., Li, S., Zhuang, B., Li, M., 2016. Integrated studies of a regional ozone  
603 pollution synthetically affected by subtropical high and typhoon system in the Yangtze River Delta region, China. *Atmos.*  
604 *Chem. Phys.* 16, 15801-15819.

605 Stein, A.F., Draxler, R.R., Rolph, G.D., Stunder, B.J.B., Cohen, M.D., Ngan, F., 2015. NOAA's HYSPLIT Atmospheric Transport  
606 and Dispersion Modeling System. *Bulletin of the American Meteorological Society* 96, 2059-2077.

607 Steinhoff, D.F., Bromwich, D.H., Speirs, J.C., McGowan, H.A., Monaghan, A.J., 2014. Austral summer foehn winds over the  
608 McMurdo dry valleys of Antarctica from Polar WRF. *Quarterly Journal of the Royal Meteorological Society* 140, 1825-1837.

609 Stull, R.B., 1988. *An Introduction to Boundary Layer Meteorology*; Kluwer Academic Publishers, Dordrecht, The  
610 Netherlands.

611 Tang, G., Zhang, J., Zhu, X., Song, T., Münkel, C., Hu, B., Schäfer, K., Liu, Z., Zhang, J., Wang, L., Xin, J., Suppan, P., Wang, Y.,  
612 2016. Mixing layer height and its implications for air pollution over Beijing, China. *Atmos. Chem. Phys.* 16, 2459-2475.

613 Wang, X.Y., Wang, K.C., 2014. Estimation of atmospheric mixing layer height from radiosonde data. *Atmos. Meas. Tech.* 7,  
614 1701-1709.

615 Wu, W., Fu, T.-M., Arnold, S.R., Spracklen, D.V., Zhang, A., Tao, W., Wang, X., Hou, Y., Mo, J., Chen, J., Li, Y., Feng, X., Lin, H.,  
616 Huang, Z., Zheng, J., Shen, H., Zhu, L., Wang, C., Ye, J., Yang, X., 2024. Temperature-Dependent Evaporative Anthropogenic  
617 VOC Emissions Significantly Exacerbate Regional Ozone Pollution. *Environmental Science & Technology* 58, 5430-5441.

618 Xu, J., Zhang, Z., Zhao, X., Zhang, J., 2024. Synthetically impacts of the topography and typhoon periphery on the  
619 atmospheric boundary layer structure and special regional pollution pattern of O<sub>3</sub> in North China Plain. *Atmospheric*  
620 *Environment* 330, 120566.

621 Xu, X., Shu, S., Wang, G., Li, W., 2026. Machine-learning-based identification of influencing factors and synoptic patterns

622 of foehn on the eastern foothills of the Taihang Mountains, China. *Atmos. Chem. Phys.* 26, 6507-6519.

623 Yang, X., Yang, M., Li, J., Zhang, S., 2018. Impact analysis of a Taihang Mountain foehn on haze intensity. *Meteorol. Monthly*

624 (in Chinese) 44, 313-319.

625 Zhang, Q., Streets, D.G., Carmichael, G.R., He, K.B., Huo, H., Kannari, A., Klimont, Z., Park, I.S., Reddy, S., Fu, J.S., Chen, D.,

626 Duan, L., Lei, Y., Wang, L.T., Yao, Z.L., 2009. Asian emissions in 2006 for the NASA INTEX-B mission. *Atmos. Chem. Phys.* 9,

627 5131-5153.

628 Zhang, S., Zeng, G., Yang, X., Wu, R., Yin, Z., 2021. Comparison of the influence of two types of cold surge on haze

629 dispersion in eastern China. *Atmos. Chem. Phys.* 21, 15185-15197.

630 Zong, L., Yang, Y., Xia, H., Yuan, J., Guo, M., 2023. Elucidating the Impacts of Various Atmospheric Ventilation Conditions

631 on Local and Transboundary Ozone Pollution Patterns: A Case Study of Beijing, China. *Journal of Geophysical Research:*

632 *Atmospheres* 128, e2023JD039141.

633